energies

MDPI

Article

Magnetic Field during Wireless Charging in an Electric Vehicle According to Standard SAE J2954

Tommaso Campi [1,*], Silvano Cruciani [1], Francesca Maradei [2] and Mauro Feliziani [1]

[1] Department of Industrial and Information Engineering and Economics, University of L'Aquila, 67100 L'Aquila, Italy; silvano.cruciani@univaq.it (S.C.); mauro.feliziani@univaq.it (M.F.)
[2] Department of Astronautics, Electrical and Energetics Engineering, Sapienza University of Rome, 00184 Rome, Italy; francesca.maradei@uniroma1.it
* Correspondence: tommaso.campi@univaq.it; Tel.: +39-0862-434-421

Received: 23 April 2019; Accepted: 8 May 2019; Published: 11 May 2019

Abstract: The Society of Automotive Engineers (SAE) Recommended Practice (RP) J2954 (November 2017) was recently published to standardize the wireless power transfer (WPT) technology to recharge the battery of an electric vehicle (EV). The SAE J2954 RP establishes criteria for interoperability, electromagnetic compatibility (EMC), electromagnetic field (EMF) safety, etc. The aim of this study was to predict the magnetic field behavior inside and outside an EV during wireless charging using the design criteria of SAE RP J2954. Analyzing the worst case configurations of WPT coils and EV bodyshell by a sophisticated software tool based on the finite element method (FEM) that takes into account the field reflection and refraction of the metal EV bodyshell, it is possible to numerically assess the magnetic field levels in the environment. The investigation was performed considering the worst case configuration—a small city car with a Class 2 WPT system of 7.7 kVA with WPT coils with maximum admissible ground clearance and offset. The results showed that the reference level (RL) of the International Commission on Non-Ionizing Radiation Protection (ICNIRP) guidelines in terms of magnetic flux density was exceeded under and beside the EV. To mitigate the magnetic field, the currents flowing through the WPT coils were varied using the inductor-capacitor-capacitor (LCC) compensation instead of the traditional series-series (SS) compensation. The corresponding calculated field was compliant with the 2010 ICNIRP RL and presented a limited exceedance of the 1998 ICNIRP RL. Finally, the influence of the body width on the magnetic field behavior adopting maximum offset was investigated, demonstrating that the magnetic field emission in the environment increased as the ground clearance increased and as the body width decreased.

Keywords: electric vehicles; electromagnetic compatibility; electromagnetic fields safety; LCC compensation; magnetic field; wireless power transfer

1. Introduction

In the future, electric vehicles (EVs) are expected to become the most widely used vehicles due to the increasing demand for reduction of exhaust gas emissions. The electric powertrains are much better than the traditional internal combustion engines in terms of environmental impact, and they lead to a significant reduction of costs and emissions. Nowadays, the EV battery charging is performed via plug-in (conductive) connection. However, in the future, autonomous drive systems will require automatic battery recharge without any human intervention. To this aim, wireless charging is a very suitable solution. The vision is that, in a few years, the EVs will be charged by inductively-based wireless power transfer (WPT) [1–4] technology. For a driver or an advanced driver assistant, it will be enough to park the vehicle equipped with a receiving circuit in a parking space suitably equipped with a transmitting circuit in order to recharge the EV battery. Obviously, it is of paramount importance to

have full interoperability between different vehicles and different parking slots with WPT technology. Standardization of WPT systems is therefore required.

Currently, the automotive WPT technology for EVs is standardized by International Organization for Standardization (ISO) 19363 [5], International Electrotechnical Commission (IEC) 61980 [6], and the Society of Automotive Engineers (SAE) J2954 [7], but the standardization work is still in progress, as many issues still need to be addressed. The SAE Recommended Practice (RP) J2954 and other related documents establish an industry-wide specification that defines acceptable criteria for interoperability, electromagnetic compatibility (EMC), electromagnetic fields (EMF) safety, minimum performance, and safety and testing for wireless charging of light duty EVs [7,8].

One of the main issues that needs to be addressed before the WPT technology is commercialized is the compliance with the EMF safety standards and regulations [9,10] for people located inside the vehicle (passengers) or in close proximity (pedestrians) while the wireless charging process is occurring. A near-field WPT system is based on two inductively coupled coils, and the wireless power transfer takes place as in the transformers but with the presence of a significant air gap given by the ground clearance. Indeed, in automotive application, the transmitting coil is placed on the ground while the receiving coil is placed on the car underbody. The coupling factor k between coils depends on the coil design, the separation distance between the coils, and their possible lateral misalignment. It can often be very small ($k << 1$), and therefore the magnetic flux leakage in the environment can be very high. In this work, the magnetic field level produced by a WPT charging system applied to a city-car with the coil configuration as recommended by SAE standard was numerically assessed and compared with EMF safety limits. Several configurations were tested by simulations after experimental validation to verify the influence of the coil vertical separation and the lateral misalignment. Additionally, the impact of the body dimension on the magnetic field emission was investigated. Finally, the use and the tuning of the inductor-capacitor-capacitor (LCC) compensation was presented to reduce the magnetic field without affecting the WPT electrical performances.

2. Magnetic Field Configuration According to SAE Recommended Practice J2954

Using the SAE RP J2954 terminology, a typical WPT system consists of a ground assembly (GA), i.e., a primary (or a transmitting) circuit, and a vehicle assembly (VA), i.e., a secondary (or a receiving) circuit. The GA and the VA are both composed of the electronic unit and the coil. In the electronic unit of the GA, there are all the components required for the power conversion of the alternating current (AC) electric grid quantities for the power supply of the transmission coil at high frequency, i.e., a power factor correction (PFC) converter to rectify and adjust the level of the input voltage and a high frequency inverter for the direct current- (DC) AC conversion compensation capacitors. In the electronic unit of the VA, there are the compensation capacitors, the rectifier for the AC-DC conversion, and the battery charger [7].

The operational nominal frequency is fixed by WPT standards to f = 85 kHz (tuning band 81.38 to 90 kHz), and the admissible power levels for light-duty vehicles are divided by SAE in four classes: WPT1 = 3.7 kVA, WPT2 = 7.7 kVA, WPT3 = 11.1 kVA, and WPT4 = 22 kVA. Additionally, the efficiency η is standardized: $\eta > 85\%$ for aligned coils, $\eta > 80\%$ for misaligned coils (offset position).

The vertical separation between GA and VA coils plays an important role as the coupling factor k decreases and the ground clearance increases. Thus, three Z-classes are defined to classify the WPT systems based on the expected maximum ground clearance as: Z1 = 100–150 mm, Z2 = 140–210 mm, and Z3 = 170–250 mm. Also, the offset position is standardized with respect to the optimal position, which coincides with the centers of circular GA and VA coils when they are aligned. The WPT system operates at maximum efficiency when the coils are in optimal position. The maximum admissible offset is ± 75 mm in the fore and aft direction (x axis) and ± 100 mm in the lateral direction (y axis).

In a real scenario, the GA coil will be mounted in the ground floor and the VA coil in the vehicle underbody. The configuration is not fixed, as it depends on the WPT class of the EV charging system, on the ground clearance that varies with the kind of vehicle and its load weight, and on the offset

position due to an imprecise parking. Any variation from the optimal position leads to a decrease of the coupling factor k with a consequent increase of the magnetic field emission. Other parameters playing an important role in the magnetic field distribution are the dimension, the shape, and the material of the EV bodyshell. Indeed, the most critical region (with exclusion of the entire area underneath the vehicle, which is protected by an access control system) for EMF safety is the region beside the vehicle at a short distance from the ground. For a given WPT class, the magnetic field is maximum for small size vehicles with maximum ground clearance and maximum offset.

The goal of this study was to numerically predict the magnetic field in the environment [11–24]. The numerical simulations were carried out by a hybrid technique based on the solution of an electromagnetic (EM) field/circuit coupled problem. As a secondary goal, the mitigation of the magnetic field emissions was addressed by using an LCC compensation [25–29] to control the coil currents in order to be compliant with EMF safety regulations. Since the main focus was to assess the most critical magnetic field in the environment, the worst case EV-WPT system configuration was considered herein, e.g., small size vehicle (city car), high power level for the considered vehicle (WPT Class 2), maximum ground clearance, and maximum offset.

3. WPT Equivalent Circuit and Compensation Networks

The analysis of the WPT system could be performed using a simplified equivalent circuit where the primary (GA) and the secondary (VA) coils were modeled by two coupled inductors, the electric power generation block was modeled by a simple voltage sinusoidal source, and the load was modeled by a resistive load. The inductive circuit was placed in resonant condition by using (at least) two capacitors in order to increase the power transfer that otherwise would be very small due to the low coupling factor k. In the following analysis, two compensation topologies were considered—series-series (SS) and double sided LCC [25–29].

The SS compensation is very popular for WPT applications for its simplicity, low cost, and high performance. It is simply obtained by connecting, in series, a compensation capacitor to both GA and VA coils modeled by a series resistance and inductance. The LCC compensation has already been proposed for a number of applications. It consists of using two capacitors (C_s, C_f) and one inductor (L_f) for both GA and VA sides in order to compensate the reactive power of the coils inductance. A sketch of series and LCC compensation circuits that should be used for both GA and VA coils are shown in Figure 1.

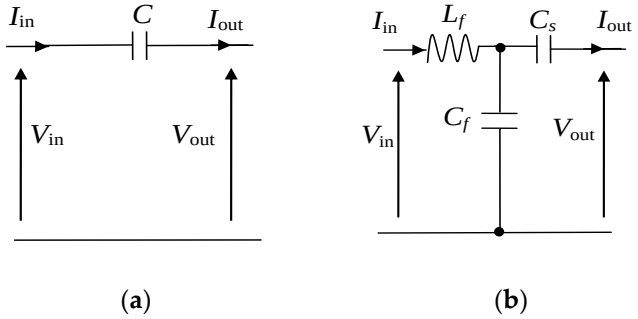

Figure 1. Series (**a**) and inductor-capacitor-capacitor (LCC) (**b**) compensation circuits used for each circuit side [i.e., ground assembly (GA) and vehicle assembly (VA) coils].

The simplified equivalent circuit for a WPT system with SS compensation topology is shown in Figure 2a, where V_S and R_S represent the GA source voltage and its internal resistance, R_L is the equivalent resistive load, R_{GA} and L_{GA} are the GA coil resistance and the self-inductance, R_{VA} and L_{VA}

are the VA coil resistance and the self-inductance, and M is the mutual inductance between GA and VA coils. The SS compensation capacitors C_{GA} and C_{VA} are given by:

$$C_{GA} = \frac{1}{\omega_0^2 L_{GA}} \tag{1a}$$

$$C_{VA} = \frac{1}{\omega_0^2 L_{VA}} \tag{1b}$$

where $\omega_0 = 2\pi f_0$ is the angular frequency and f_0 is the resonant frequency (f_0 = 85 kHz for automotive WPT).

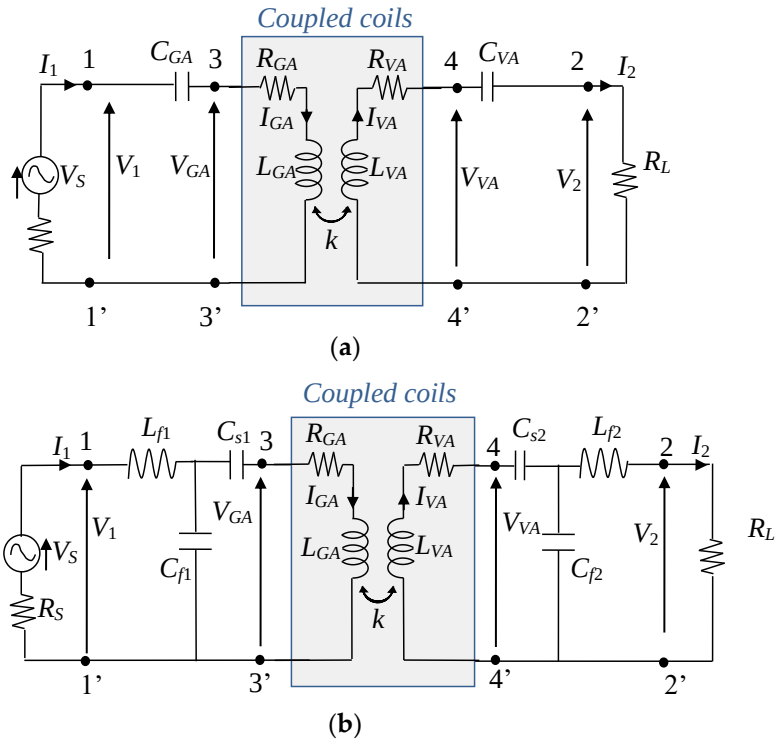

Figure 2. Equivalent simplified circuit of a wireless power transfer (WPT) system with series-series (SS) (**a**) and LCC (**b**) compensation topologies.

The equivalent circuit adopting the double side LCC compensation topology is shown in Figure 2b [25–29]. The parameters of the equivalent circuit are related by the following equations:

$$L_{f1}C_{f1} = \frac{1}{\omega_0^2} \tag{2a}$$

$$L_{f2}C_{f2} = \frac{1}{\omega_0^2} \tag{2b}$$

$$L_{GA} - L_{f1} = \frac{1}{\omega_0^2 C_{s1}} \tag{2c}$$

$$L_{VA} - L_{f2} = \frac{1}{\omega_0^2 C_{s2}} \tag{2d}$$

The values of L_{f1} and L_{f2} are chosen as the functions of the voltages at the input and the output ports, V_1 and V_2, respectively, of the output real power P_2, and of the coupling factor k [29]. The procedure for the calculation of L_{f1} and L_{f2} is described in the following.

The efficiency η is defined as the ratio between the output real power P_2 at port 2-2′, which is basically the power on the load resistance R_L, and the input real power P_1 at port 1-1′ (see Figure 2), and it is given by:

$$\eta = \frac{P_2}{P_1} = \frac{real(Z_{22'})|I_2|^2}{real(Z_{11'})|I_1|^2} = \frac{R_L|I_2|^2}{real(Z_{11'})|I_1|^2} \tag{3}$$

where $Z_{11'}$ and $Z_{22'}$ are the input impedances at the port 1-1′ and 2-2′, and$|I_1|$and $|I_2|$ are the root mean square (rms) values of the input and output currents, respectively.

For the SS configuration, the input impedance at the port 1-1′ at resonance is given by:

$$Z_{11',ss} = R_{GA} + \frac{\omega_0^2 M^2}{R_{VA} + R_L} \tag{4}$$

and it is a real quantity, i.e., $real(Z_{11',ss}) = Z_{11',ss}$. After simple mathematical manipulations of the equations for the circuit of Figure 2a, the efficiency η_{ss} at resonance is obtained as [29]:

$$\eta_{ss} = \frac{\omega_0^2 M^2}{\left(1 + \frac{R_{VA}}{R_L}\right)\left(R_{GA}(R_{VA} + R_L) + \omega_0^2 M^2\right)} \tag{5}$$

In this case, the optimal value of the load resistance $R_{L,opt}$ that maximizes the efficiency η_{ss} is obtained from $\partial\eta_{ss}/\partial R_L = 0$, and it is given by:

$$R_{L,opt} = \omega_0 M \sqrt{\frac{R_{VA}}{R_{GA}} + \left(\frac{R_{VA}}{\omega_0 M}\right)^2} \tag{6}$$

When considering the double-side LCC compensation topology, the equivalent input impedance $Z_{44'}$ at the port 4-4′ is given at resonance by the ratio of V_{VA} and I_{VA} (see Figure 2b):

$$Z_{44'} = \frac{V_{VA}}{I_{VA}} = R_L{}' - j\frac{1}{\omega_0 C_{f2}} - j\frac{1}{\omega_0 C_{s2}} \tag{7}$$

where

$$R_L{}' = \frac{(\omega_0 L_{f2})^2}{R_L} \tag{8}$$

Impedance $Z_{44'}$ in (7) can be seen as the series connection of a resistor $R_L{}'$, a capacitor C_{f2}, and a capacitor C_{s2} [29]. Thus, it can be easily deduced that the right side of the SS compensated circuit in Figure 1a can be also used for the LCC compensation when replacing the effective load R_L in (4) with the equivalent load $R_L{}'$ given by (8) and the capacitor C_{VA} with the series of C_{s2} and C_{f2}.

With a few mathematic manipulations applied to the circuit equations, the input impedance $Z_{11',LCC}$ at port 1-1′ for the LCC configuration is given at resonance by:

$$Z_{11',LCC} = \left(\omega_0 L_{f1}\right)^2 \frac{1}{R_{GA} + \frac{\omega_0^2 M^2 R_L}{R_L R_{VA} + \omega_0^2 {L_{f2}}^2}} \tag{9}$$

Similarly to the SS compensation, the input impedance at port 1-1′ in (9) is a real quantity, i.e., $real(Z_{11',LCC}) = Z_{11',LCC}$.

The efficiency η_{LCC} for the LCC compensation can be obtained by manipulations of the equations related to the circuit of Figure 2b. It can be demonstrated that the expression of η_{LCC} is identical to that in (5) when replacing R_L with the expression (8) of $R_L{}'$, and it is given by:

$$\eta_{LCC} = \frac{\omega_0^2 M^2}{\left(1 + \frac{R_{VA} R_L}{\omega_0^2 {L_{f2}}^2}\right)\left(R_{GA}\left(R_{VA} + \frac{\omega_0^2 {L_{f2}}^2}{R_L}\right) + \omega_0^2 M^2\right)} \tag{10}$$

The optimal value of L_{f2} for maximizing the efficiency η_{LCC} can be obtained in analogy with the analysis previously described for the SS compensation. In particular, by comparing (5) with (10) when assuming the optimum load $R_{L,opt}$ (6), it is possible to find the value of L_{f2} that allows us to reach the maximum efficiency η_{LCC} in case of LCC compensation for a given value of the load resistance R_L as:

$$L_{f2} = \frac{\sqrt{R_L R_L{}'}}{\omega_0} = \sqrt{R_L \frac{M}{\omega_0}} \sqrt[4]{\frac{R_{VA}}{R_{GA}} + \left(\frac{R_{VA}}{\omega_0 M}\right)^2} \tag{11}$$

The LCC configuration is particularly suitable to regulate the values of the current ratio I_{VA}/I_{GA} according to the desired target. In particular, the coil current ratio I_{VA}/I_{GA} at resonance is given by:

$$\frac{I_{VA}}{I_{GA}} = \frac{j\omega_0 M}{R_{VA} + j\omega_0 L_{f2} + Z_{44'}} = \frac{j\omega_0 M}{R_{VA} + \left(\omega_0 L_{f2}\right)^2 / R_L} \tag{12}$$

From (12), it is evident that the ratio of coil currents I_{VA}/I_{GA} can be modified by simply varying the value of the inductance L_{f2}.

From (9), it can be observed that any variation of the inductance L_{f1} affects the input impedance $Z_{11',LCC}$, as shown in Figure 3. Therefore, L_{f1} can be selected with a value that is the most suitable for the required power transfer without affecting the efficiency η_{LCC} in (10).

Finally, it is worth noting that the equations described above do not take into account the equivalent series resistances (ESRs) of the reactive circuit parameters, i.e., inductors and capacitors are assumed to be ideal without any power loss. Considering the ESR resistances, the equations would be more complex. However, the circuit analysis considering only ideal inductances and capacitances still provides a good approximation of the circuit behavior in the first step of the WPT system design.

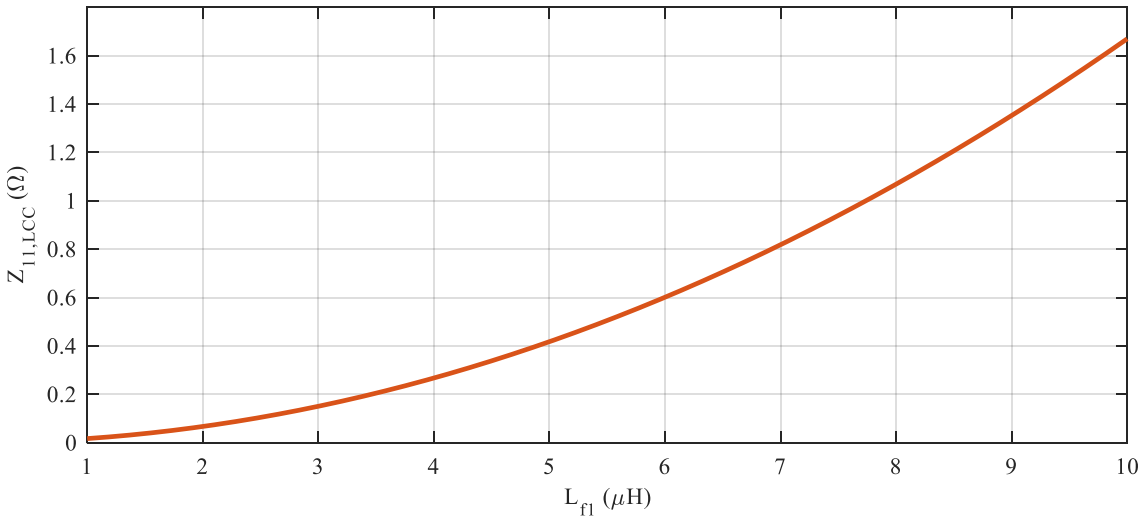

Figure 3. Input impedance $Z_{11',LCC}$ versus inductance L_{f1} (class Z3, aligned coils with the configuration shown in Section 5 in Figures 4 and 5).

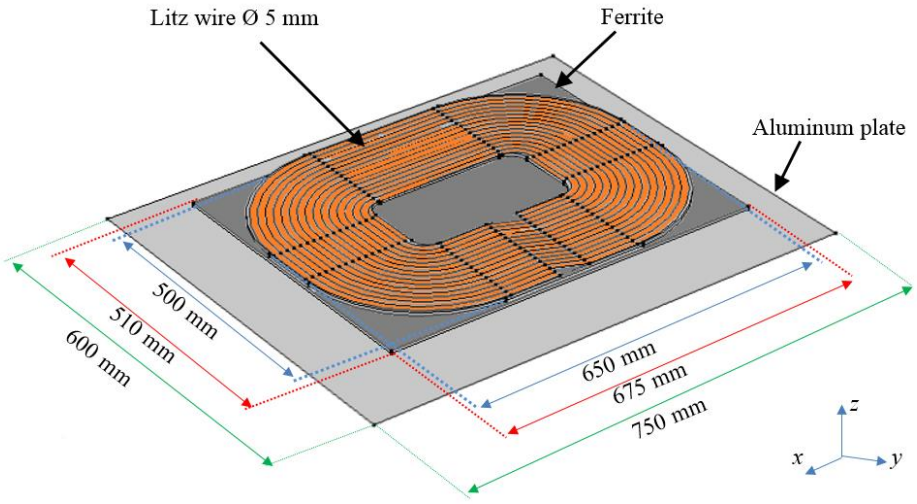

Figure 4. Electro-geometrical configuration of the GA coil.

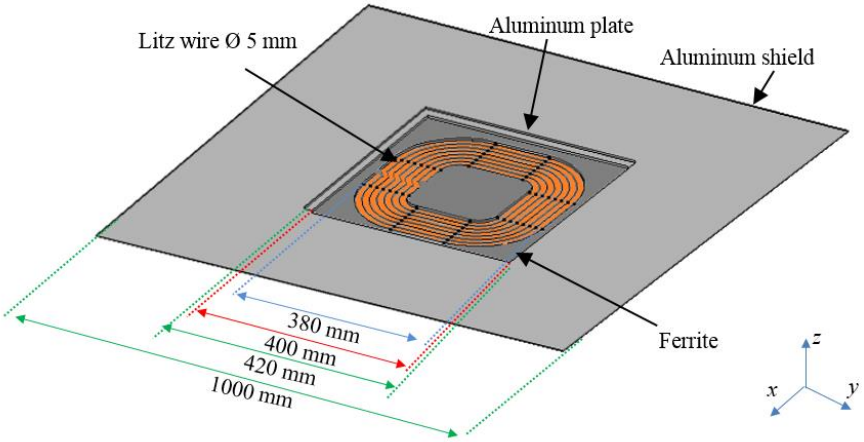

Figure 5. Electro-geometrical configuration of the VA coil.

4. Simulation Model

4.1. Field Equations

The magnetic field can be calculated in the frequency domain by solving the magneto-quasi static (MQS) equations that, in terms of potentials $\boldsymbol{A}$-V, are given by:

$$\nabla \times \frac{1}{\mu} \nabla \times \boldsymbol{A} + j\omega\sigma\boldsymbol{A} + \sigma\nabla V = \boldsymbol{J_s} \tag{13}$$

$$\nabla \cdot (j\omega\sigma\boldsymbol{A} + \sigma\nabla V - \boldsymbol{J_s}) = 0 \tag{14}$$

where $\boldsymbol{B}$ is the magnetic flux density, $\boldsymbol{A}$ is the magnetic vector potential, V is the electric potential, $\boldsymbol{J_s}$ is the source current density, μ is the magnetic permeability, and σ is the electrical conductivity. The electric field $\boldsymbol{E}$ and the magnetic flux density $\boldsymbol{B}$ are related to the potentials $\boldsymbol{A}$-V by:

$$\boldsymbol{B} = \nabla \times \boldsymbol{A} \tag{15}$$

$$\boldsymbol{E} = -j\omega\boldsymbol{A} - \nabla V \tag{16}$$

When modeling the electromagnetic field propagation inside a conductive media, the induced eddy currents are mostly located in the outer layer of thickness δ called skin depth, given by:

$$\delta = 1/\sqrt{\pi f \mu \sigma} \tag{17}$$

This phenomenon is known as skin effect. In order to properly model the skin effect by numerical methods based on a partial differential equations solution, the conductive regions must be finely discretized, i.e., the mesh element dimension h must be much smaller than δ. This fine discretization can lead to a very high number of finite elements, and thus the solution can be very heavy or impractical [30–32]. To overcome this issue, suitable numerical techniques can be adopted. To this aim, two different options exist—the conductive thin region with small thickness t is assumed to be quite impenetrable ($t >> \delta$, negligible transmission through the conductive region) or highly penetrable ($t << \delta$, relevant transmission through the conductive region). In the first case, to reduce the number of elements necessary to discretize the EV bodyshell, impedance boundary conditions (IBCs) [33] can be used to calculate the magnetic field outside the vehicle when $t >> \delta$. Using IBCs, the three-dimensional (3D) bodyshell is eliminated from the computational domain, and it is substituted by a boundary surface where IBCs are imposed. By this procedure, only the field reflection outside the vehicle is accounted for, while no information is obtained on the transmitted field inside the cabin that is considered negligible. In order to consider the magnetic field inside the vehicle, impedance network boundary conditions (INBCs) [34,35] or artificial material single layer (AMSL) [36–38] methods can be used. Both these techniques take into account the field transmitted through the bodyshell in the vehicle. The INBCs are an extension of IBCs to take into account the field penetration through thin conductive layers. As in the IBCs implementation, the bodyshell is eliminated from the computational domain and replaced by a field discontinuity interface, where the coupled boundary conditions INBCs are imposed to assure the continuity of the electric and the magnetic field tangential components on both conductive layer surfaces. The formulation of the AMSL method is completely different from that of the INBC method, even if the scope is very similar. The AMSL method consists of replacing the physical constants of the thin layer region with those of an artificial material that no longer requires a fine discretization but takes into account exactly the field penetration through the shield when it is discretized by a single layer of finite elements along the direction of propagation. The main practical difference between AMSL and INBC methods is that, in the first method, the real geometrical configuration of the thin layer is maintained in the computational domain, while in the second, the thin conductive layer is eliminated from the domain, modifying the geometrical configuration. The AMSL method, formulated using both first [36] and second order (more precise) [37] finite element interpolation functions, can be used also to model anisotropic media [38]. The results conveyed in this paper were achieved by adopting the second order AMSL method [37].

4.2. Circuit Parameters Extraction

The equivalent circuit parameters in terms of self-inductances L_{VA} and L_{GA}, mutual inductance M, and coupling factor k can be extracted by 3D finite element method (FEM) simulations via the magnetic energy W_m. This last factor is calculated in the entire computational domain Ω from the magnetic field $\boldsymbol{H}$ and the conjugate $\boldsymbol{B}^*$ of the magnetic flux density obtained by FEM simulations. The magnetic energy W_m is defined as:

$$W_m = \frac{1}{2}\int_{\Omega} \boldsymbol{H} \cdot \boldsymbol{B}^* d\Omega \tag{18}$$

The self-inductances L_{VA} and L_{GA}, and the mutual inductance M are obtained from W_m when the currents I_{VA} and I_{GA} flowing through the coils are imposed in the field simulations as:

$$L_{GA} = \frac{2W_{m,GA}}{|I_{GA}|^2}, \qquad W_{m,GA} \text{ calculated when } I_{GA} = 1, \quad I_{VA} = 0 \tag{19a}$$

$$L_{VA} = \frac{2W_{m,VA}}{|I_{VA}|^2} \quad , \qquad W_{m,VA} \text{ calculated when } I_{GA} = 0, \quad I_{VA} = 1 \tag{19b}$$

$$M = \frac{W_{m,a} - W_{m,b}}{2|I_{GA}||I_{VA}|} \quad \begin{matrix} case\ a) W_{m,a} \text{ calculated when } I_{GA} = 1, I_{VA} = 1 \\ case\ b) W_{m,b} \text{ calculated when } I_{GA} = 1, I_{VA} = -1 \end{matrix} \tag{19c}$$

The coupling factor k between the two coils is defined as:

$$k = \frac{M}{\sqrt{L_{GA}L_{VA}}} \tag{20}$$

The AC resistances of the coils made by Litz wire, R_{GA} and R_{VA}, were taken from the Litz wire datasheet at 85 kHz. Their values are generally very similar to those of the DC resistances.

5. Applications

5.1. WPT Systems

A demonstrative WPT system was designed and simulated to calculate the performances and the magnetic field emission. The considered system was designed to work at the WPT2 power level (7.7 kVA) and for the maximum ground clearance Z3 = 170–250 mm. The GA coil was assumed to be at zero level from the ground (z = 0), similar to a flush ground mounting position [7]. A scheme of the GA coil is reported in Figure 4. The spiral wound coil was composed of two parallel wires with N_1 = 8 turns. In order to reduce the AC power losses in the copper conductors, a Litz wire was adopted. It was composed of 1260 strands of American wire gauge (AWG) 38 insulated wires. The equivalent section from an electrical point of view was identical to that of a cylindrical conductor with an external diameter of Ø = 5 mm. To improve the coupling factor k and to reduce the magnetic flux leakage, a magnetic shield composed of ferrite tiles was placed under the winding. The ferrite shield substantially reduced the eddy currents in external metallic objects as the EV bodyshell. A conductive aluminum plate was placed under the ferrite shield to further mitigate the magnetic field emissions. There was no separation distance between the GA winding and the magnetic shield, while a space $s_{m,GA}$ = 30 mm was considered between the magnetic shield and the aluminum plate that was filled by a nonconductive material. The coil specifications are reported in Table 1.

Table 1. Electro-geometrical configuration of the considered WPT coils.

Outer Dimension	*GA*			*VA*		
	Length (mm)	**Width (mm)**	**Thickness (mm)**	**Length (mm)**	**Width (mm)**	**Thickness (mm)**
Winding	650	500	5	380	380	5
Ferrite shield	675	510	5	400	400	5
Aluminum plate	750	600	2	420	420	3
Aluminum shield	/	/	/	1000	1000	2

The VA coil had a square shape with a fillet corner, and it was realized with the same type of Litz wire as that used for the GA coil. As for the VA coil, a magnetic shield made of ferrite tiles was placed over the winding to improve the coupling factor and to reduce the magnetic field leakage, and two aluminum (*Al*) layers were adopted over the ferrite to shield the magnetic field and protect the passengers in the EV cabin as well as the onboard electrical/electronic systems. There was no separation distance between the winding and the magnetic shield and between the magnetic shield and the first aluminum layer (plate), while a space $s_{c,VA}$ = 20 mm filled by a nonconductive material was considered between the aluminum plate and the second larger aluminum layer (shield). The VA coil specifications are reported in Figure 5 and Table 1.

5.2. Car Body

To evaluate the magnetic field behavior and the system performance, the presence of the car body was considered. The adopted EV was a small city car with outer dimensions of m_x = 3.46 m, m_y = 1.6 m, and m_z = 1.46 m. The distance between the front and the rear wheel axes was 2.6 m. The EV body was assumed to be made of high strength steel with an electrical conductivity of σ = 10 MS/m and a uniform thickness of t_k = 1 mm. The ground clearance was varied to reproduce two different load configurations. In the first, the vertical distance between the GA and the VA coils was set to Δz_2 = 200 mm, allowed for the Z2 and Z3 classes, while in the second configuration, the worst-case configuration was adopted with a distance of Δz_3 = 250 mm, allowed only for the Z3 class systems [7]. It was assumed that the VA coil was placed in the center of the car underbody. In general, this position is not very usual in the fore and the aft direction (x-axis) and is not important for the magnetic field behavior, which essentially depends on the distance along the y-axis from the VA coil to the outer sides of the EV body. Thus, the lateral distance of the VA coil from the closest outer side of the EV body is the most important parameter because it is the shortest one, while irrelevant differences are in the fore and the aft direction, since the distances from the front and the back of the car are generally much larger. To take into account possible misalignment between the GA and the VA coils, an offset on both x and y directions was considered, assuming $x = y = z = 0$ at the central position of the VA coil. According to [7], the maximum offset values used in the investigations were Δx = 75 mm and Δy = 100 mm. Two important parameters are the minimum distance d_y between the GA coil and the lateral side of the vehicle and the minimum distance d_x between the GA coil and the front (or back) edge of the vehicle. The quantities d_x and d_y could be obtained as:

$$d_x = \frac{m_x}{2} - \frac{l_{GA}}{2} - \Delta x \tag{21}$$

$$d_y = \frac{m_y}{2} - \frac{w_{GA}}{2} - \Delta y \tag{22}$$

where w_{GA} and l_{GA} are the width and the length of the GA coil in y- and x-directions, respectively. In case of lateral and/or frontal offset, the distances d_x and/or d_y between the outer dimensions of the GA winding and outside area decreased, thus, there was a significant increase of the magnetic field. It should be noted that the distance between the VA coil and the vehicle external sides was invariable for every offset value, since the VA coil was installed in a fixed position in the car underbody. On the contrary, the distances d_x and d_y were variable depending on the precision of the parking, i.e., offset. To better clarify the arrangement under examination, the EV-WPT coil configuration is represented in x-y and in x-z planes in Figure 6.

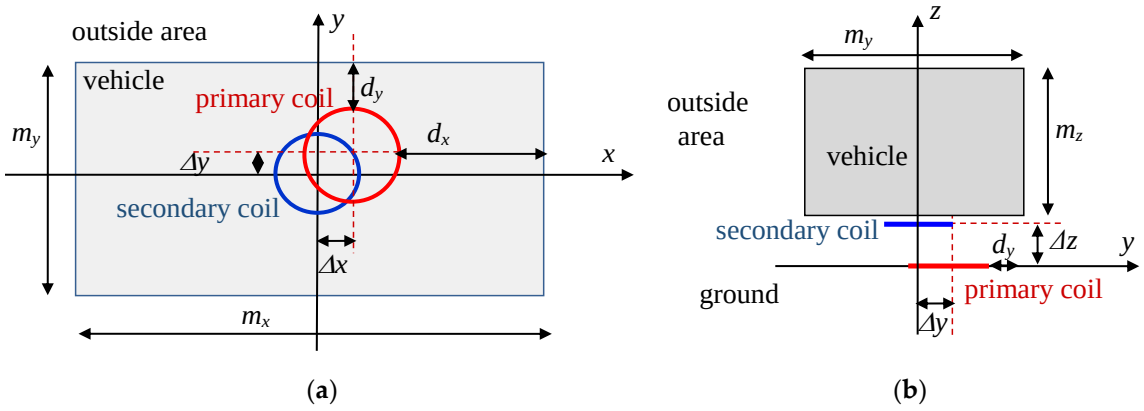

Figure 6. Sketch of the electric vehicle- (EV) WPT coil configuration in x-y plane (top view) (**a**) and in y-z plane (front view) (**b**).

A simplified car model equipped with coils as suggested by SAE RP J2954 [7] was modeled using a computer-aided design (CAD) software. Once the coils and the body were designed as shown in Figure 7, their equivalent circuit parameters in terms of self-inductances L_{VA} and L_{GA}, mutual inductance M, and coupling factor k were calculated by a 3D FEM simulation software for several offset and ground clearance configurations. The WPT system and the simplified car were meshed using a tetrahedral mesh based on second order finite elements. To reduce the number of the mesh elements, the metallic bodyshell was modeled using the AMSL method [37]. The number of mesh elements used in the simulation was 242,415, and the simulation time was 45 min and 23 s, adopting an AMD FX9350 central processing unit (CPU).

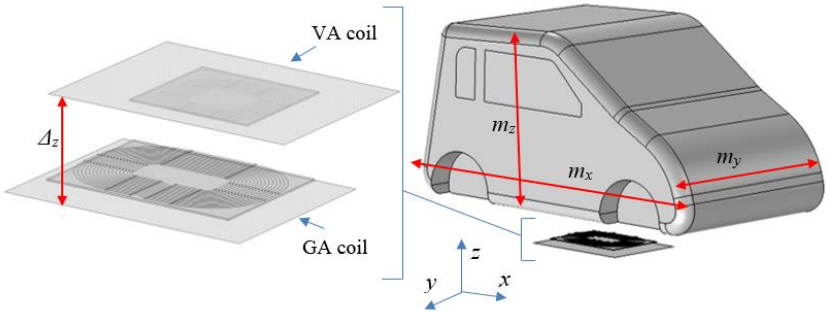

Figure 7. Computer-aided design (CAD) model of the modeled SAE J2954 coils and of the city car body with the WPT coil system.

The AC resistances of the coils made by Litz wire, R_{GA} and R_{VA}, were taken from a Litz wire datasheet at 85 kHz. For the considered length of the coils, the resistance values were R_{GA} = 22 mΩ and R_{VA} = 19 mΩ when neglecting the proximity effect. The GA and the VA coil parameters for several configurations of vertical separation and offset are reported in Table 2.

Table 2. Calculated lumped parameters of the considered WPT coils.

Δ*z* (mm)	Δ*x* (mm)	Δ*y* (mm)	L_{GA} (μH)	L_{VA} (μH)	*M* (μH)	*k*
200	0	0	50.4	39.9	6.5	0.148
200	75	0	50.6	39.9	5.75	0.131
200	75	100	50.6	40.0	4.75	0.110
250	0	0	49.2	39.1	4.5	0.102
250	75	0	49.3	39.0	3.8	0.087
250	75	100	49.3	39.0	3.2	0.072

5.3. System Performances

The evaluation of the systems performance was performed in two steps. In the first step, the simplified circuits described in Section 3 based on SS and LCC compensations were analyzed, and the obtained results were compared to find the best solution. In the second step, a more complex configuration was simulated, considering the presence of other electrical/electronic components, i.e., inverter, rectifier, and battery. The compensation capacitors and inductors were calculated according to [28,29], and their values are shown in Table 3. The load resistance was set to R_L = 25 Ω. The real power on the load resistance was fixed to $P_L = P_2$ = 7.7 kW.

Table 3. Compensation capacitors and inductors.

Compensation	C_{VA} (nF)	C_{s1} (nF)	C_{f1} (nF)	L_{f1} (μH)	C_{GA} (nF)	C_{s2} (nF)	C_{f2} (nF)	L_{f2} (μH)
SS	71.4	\	\	\	89.9	\	\	\
LCC	\	81.4	560	6.24	\	105	600	5.5

A detailed investigation on the performance of the LCC compensation was performed, adopting C_{f2} as a variable parameter, with the goal of finding the best setup when adopting the coil configuration recommended by SAE J2954. In this investigation, the maximum misalignment was considered. The distance between the coil was Δz_3 = 250 mm, and the offsets were Δx = 75 mm and Δy = 100 mm. The calculated efficiency is shown in Figure 8, where it is evident that the LCC compensation permitted the obtainment of higher efficiency compared to that of the SS compensation, $\eta_{LCC} > \eta_{SS}$, for a wide range of C_{f2} values. It is worth noting that the efficiency for the SS compensation was here obtained in case of misalignment and for a fixed value of load resistance (R_L = 25 Ω) that depended on the battery voltage and charging power, which was probably not the optimum value for the considered WPT coil configuration. On the other side, the LCC compensation easily permitted the matching of the WPT system with the load, consequently improving the overall performances.

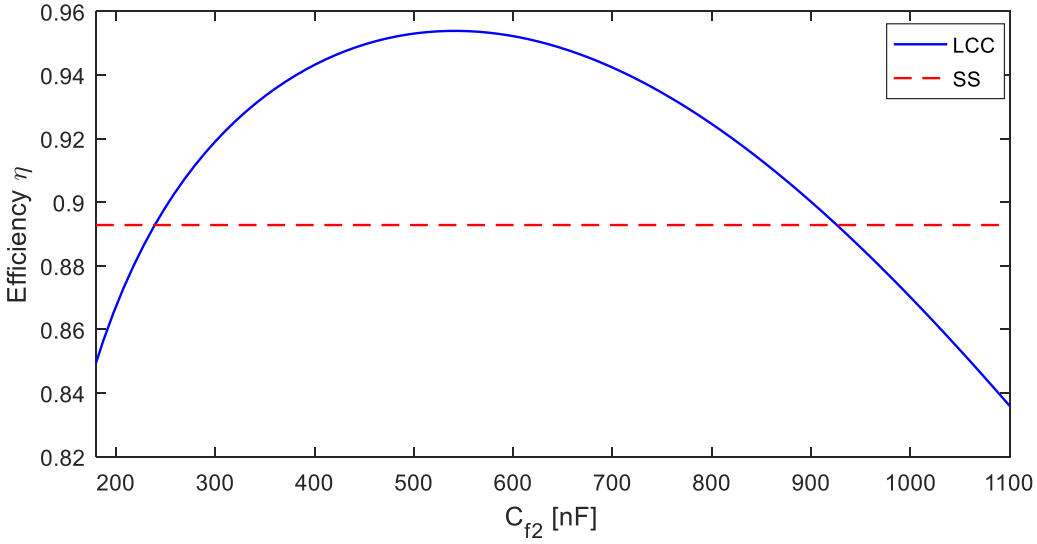

Figure 8. System efficiency η using SS compensation and LCC compensation versus variable C_{f2}.

The currents flowing through the WPT coils varying C_{f2} are shown in Figure 9, where the significant variability of the current distribution in the LCC compensation is evident. Using the SS compensation, the current I_{VA} in the VA coil was much higher than that in the GA coil (I_{GA}). Using the LCC compensation and varying C_{f2} in the range where the efficiency was very high (C_{f2} = 400 nF–600 nF), it was possible to balance the current distribution between the coils. Furthermore, the phases of GA and VA coil currents, shown in Figure 10, could be tuned by varying C_{f2}. Please note that the variation of the coil currents I_{GA} and I_{VA} had a significant effect on the magnetic field behavior, as described in the following section, especially for a significant value of the lateral offset when the GA coil was closer to the exterior side of the EV bodyshell (see Figure 6). In this case, the magnetic field was at maximum outside the EV, and this trend was enhanced when the vertical distance between coils (Z class) was at maximum. Then, the influence of the variation of the coupling factor k on the system efficiency was studied. The coupling factor was assumed to be variable in the range k = 0.07–0.148, k = 0.07 being the value corresponding to the higher vertical spacing Δz_3 = 250 mm between the coils and with maximum offset (Δx = 75 mm, Δy = 100 mm), while k = 0.148 corresponded to the lower considered spacing Δz_2 = 200 mm and without misalignment ($\Delta x = \Delta y = 0$). The graphs of the efficiency obtained for the SS compensation and for the LCC compensation with C_{f2} = 600 nF are shown in Figure 11, while the currents flowing through the coils are shown in Figure 12. The obtained results conveyed the capability of the LCC compensation to match the load for poor alignment conditions and to maintain a quasi-constant efficiency behavior for a wide range of the coupling factor values. The efficiency adopting the SS compensation was strongly influenced by the coupling condition between the coils,

with very good performance for good alignment, but there was a big degradation in the efficiency in the case of misalignment, which depended on the variable load of the vehicle and on the parking precision.

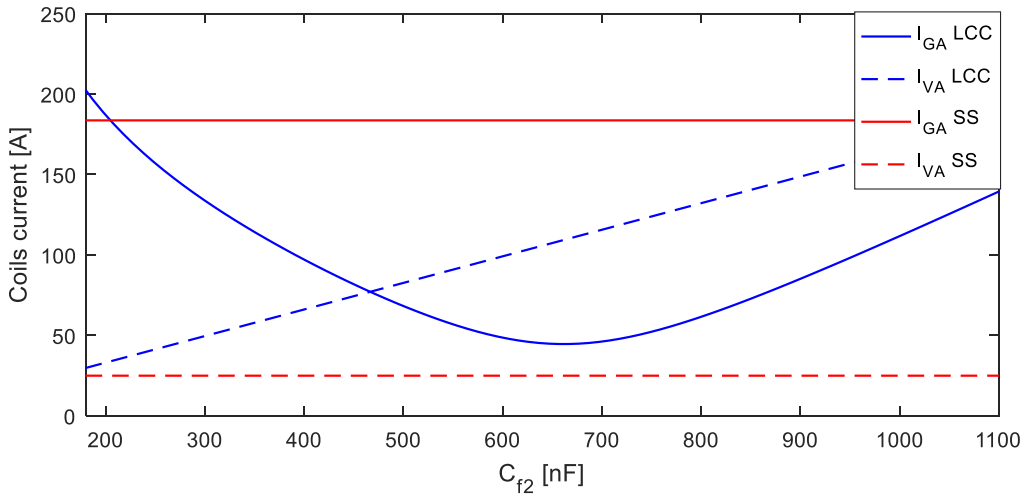

Figure 9. Coil currents distribution using SS and LCC compensations varying C_{f2}.

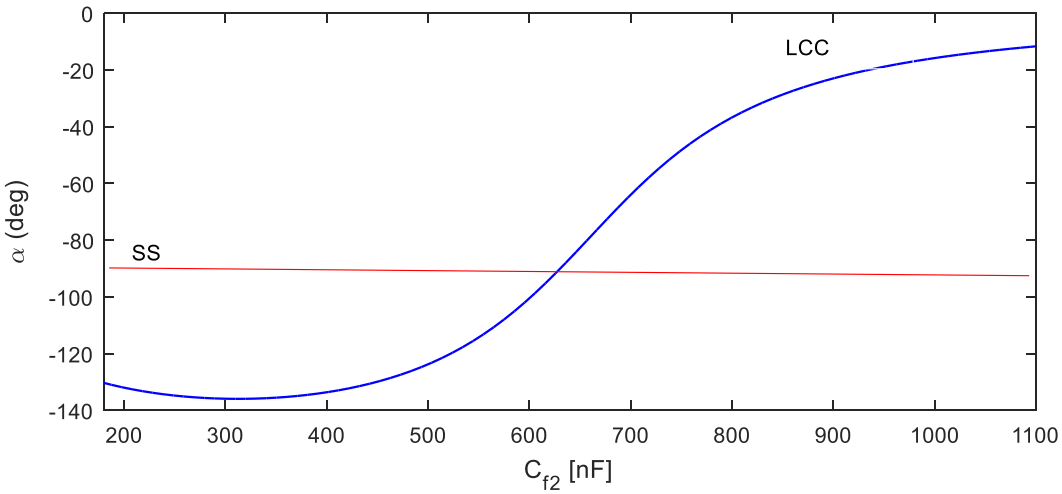

Figure 10. Phase of currents I_{GA} and I_{VA} using SS and LCC compensations varying C_{f2}.

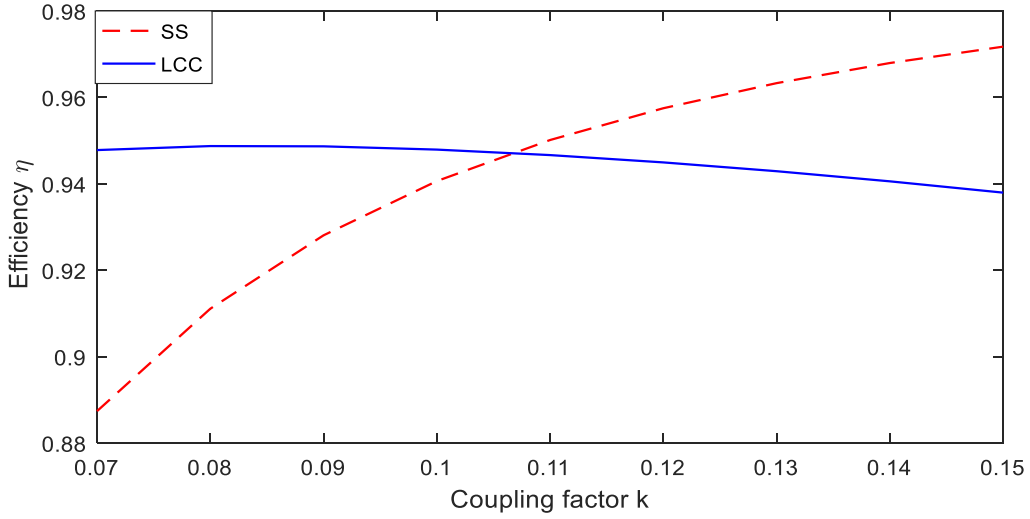

Figure 11. System efficiency using SS and LCC compensations versus coupling factor *k*.

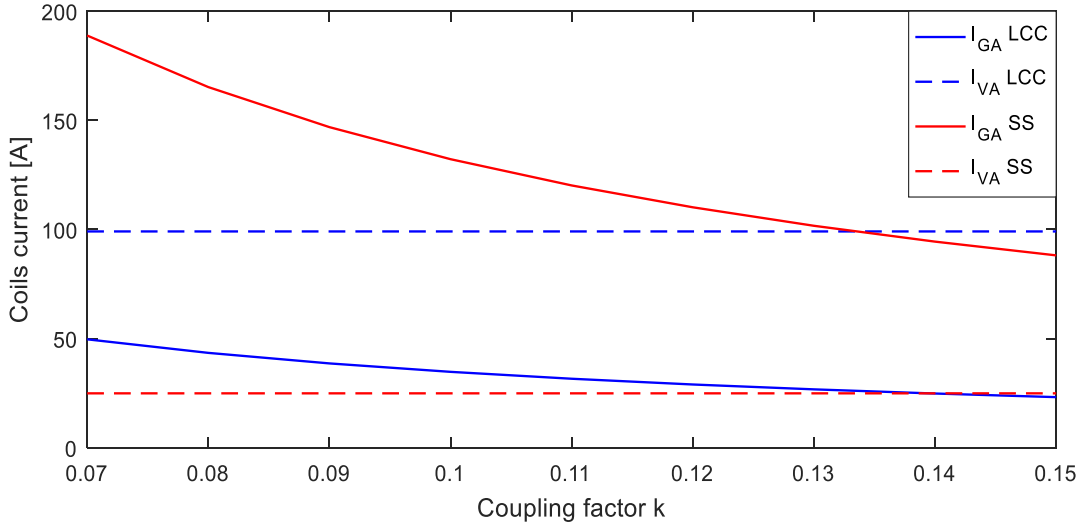

Figure 12. Coil currents (rms) distribution using SS and LCC compensations versus coupling factor *k*.

In the second step, a more realistic configuration of the WPT system (including the power conversion) was taken into account, as shown in Figure 13, where the SPICE circuit is represented for an LCC compensation. For each capacitor and inductor, an equivalent series resistance (ESR) = 5 mΩ was considered. The sinusoidal voltage source was replaced by a high frequency electronic inverter, while the load resistor was replaced by the rectifier, the filter block, and the battery. The high power square signal was generated by a MOSFETs inverter. This topology of inverter, which could be considered a D-class amplifier, permitted the reduction of losses. Specifically, there were two main losses—conduction losses and switching losses. The conduction losses were given by the on resistance $R_{ds,on}$, while the switching losses occurred during the on-off and off-on transition of the switch. In the considered application, the FCA76N60 MOSFETs were adopted. To ensure a proper driving of the switches, four independent square signals were used to pilot the MOSFETS. The driving signals of the MOSFET U1 and U3 had the same phase and were in quadrature with the driving signals of the MOSFETS U2 and U4 to obtain a pure square wave output. In order to avoid short circuit during the transition time on the same bridge leg, a dead-time dt = 2 ns was introduced. The inverter was fed from an adjustable DC voltage bus to permit the regulation of the charging power. On the receiving side, a full bridge diode rectifier was connected at the output of the compensation network to convert the high frequency voltage to a DC voltage. Schottky diodes were used to reduce conversion losses. An output filter composed of a capacitor C_{out} = 10 µF and inductance L_{out} = 10 µH was adopted to smooth the output signal. The Li-ion battery was modeled as described in [39]. In all the simulations, the battery voltage was kept fixed to V_{bat} = 310 V and the charging power fixed to P_{ch} = 7.7 kW.

Then, the system performances were calculated considering the SS compensation and the LCC compensation with C_{f2} = 600 nF. The input voltage was adjusted to obtain a charging power of P_{ch} = 7.7 kW. The overall system efficiency and the coils currents (rms values and phase shift α between I_{GA} and I_{VA}) are reported in Table 4 considering two coupling factor values—the minimum k = 0.072 and the maximum k = 0.148. From the obtained results, there were evident advantages of the LCC configuration in terms of reduction of the total coil currents and the current on the GA coil. The performance difference was less evident for the higher value of k when the vertical separation between the two coils was reduced or when offset was not considered. The current waveforms of I_{GA} and I_{VA} considering k = 0.072 for SS and LCC compensations are shown in Figures 14 and 15, respectively. The calculated coil currents were used as sources for the evaluation of the magnetic field, as described in the next section.

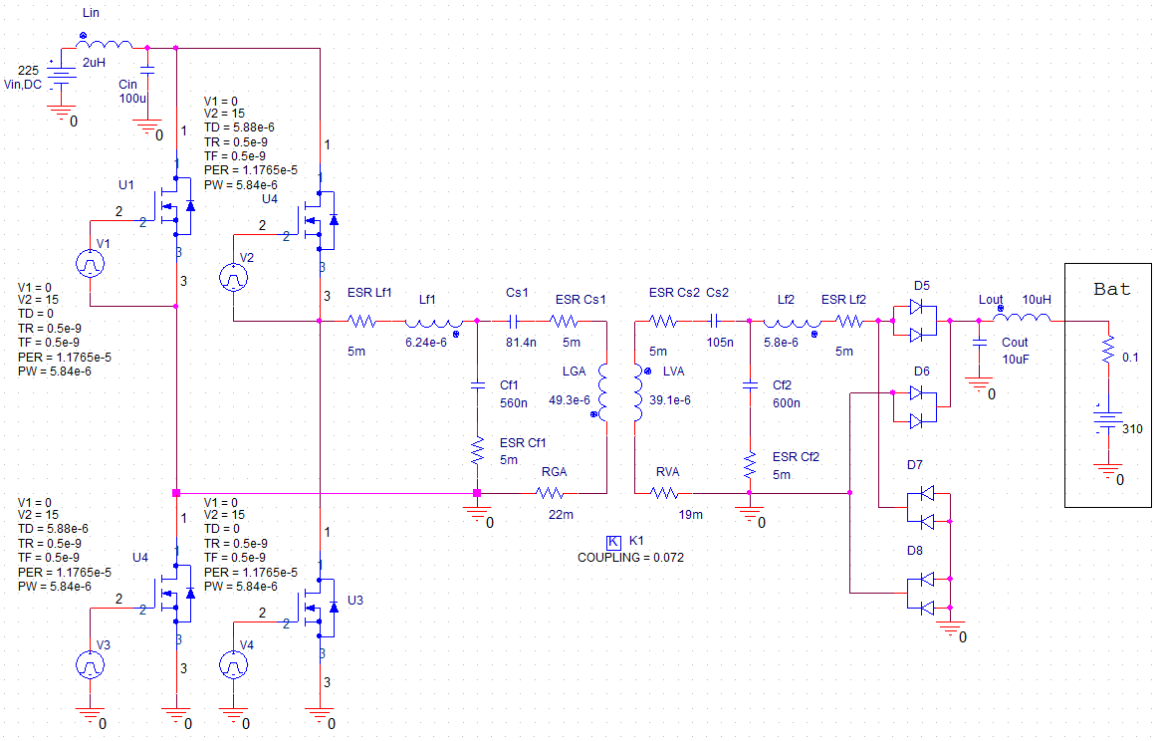

Figure 13. Equivalent circuit with electronic components and LCC compensation.

Table 4. Electrical quantities (rms) using SS and LCC compensation.

k	SS				LCC			
	I_{GA} (A)	I_{VA} (A)	η	α (deg)	I_{GA} (A)	I_{VA} (A)	η	α (deg)
0.072	177.2	28.7	0.880	82	60.2	89.5	0.915	117
0.148	125.1	28.7	0.920	81	81.6	21.3	0.922	115

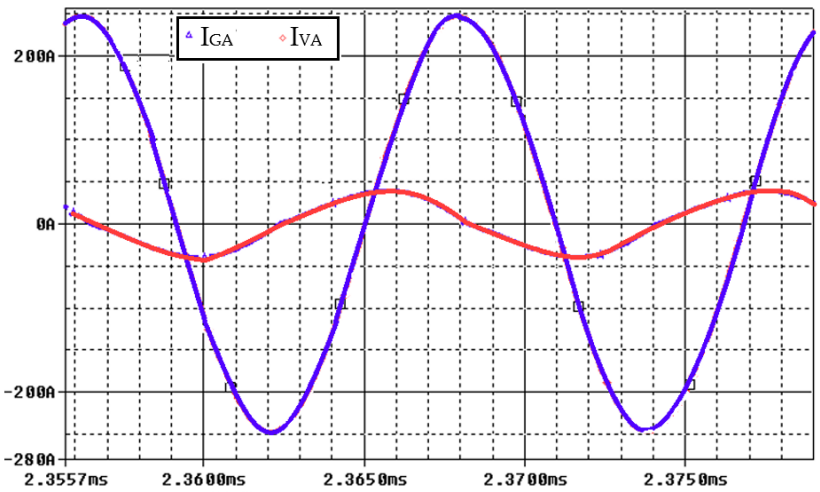

Figure 14. Waveforms of the coil currents for SS compensation.

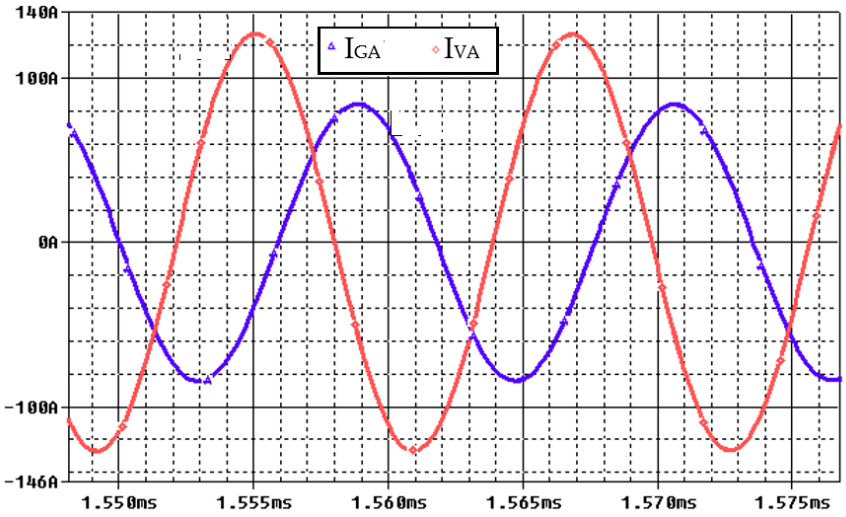

Figure 15. Waveforms of the coil currents for LCC compensation.

5.4. Magnetic Field Emission

Before performing simulations to predict the magnetic field produced by a WPT automotive system, an experimental validation of the numerical tool was carried out in the simplified configuration, shown in Figure 16. The simplified setup representing a WPT automotive scenario was composed of a current coil placed on the ground in the presence of a steel enclosure that modeled the EV bodyshell. The thickness of the steel enclosure was t_k = 1 mm. The enclosure had dimensions of m_x = 0.8 m, m_y = 0.8 m, and m_z = 0.4 m. The rectangular coil had external dimensions h_c = 35 cm and w_c = 20 cm. The vertical separation between the coil and the enclosure was Δz = 10 cm. The rectangular coil was placed at a variable distance d_y from the projection of the enclosure vertical face, d_y =10, 15, 20 cm. In the experimentation, the coil current was set to I = 5 A at 20 kHz frequency. The magnetic flux density was measured by the field sensor Wandel & Goltermann EFA-3 along two orthogonal lines, l_a and l_b, beside the aluminum enclosure, as depicted in Figure 16. The horizontal line l_a was parallel to the x axis at a distance of d_c = 100 mm from the enclosure and d_g = 100 mm from the ground. The vertical line l_b was parallel to the z axis, and the distance between the enclosure and the line was d_c = 100 mm. The magnetic flux density was also calculated by an FEM code, using the AMSL method to model the steel bodyshell. The discretization of the bodyshell required only 11,780 second order finite elements. The obtained results are reported in Figure 17, revealing a very good agreement between simulations and measurements.

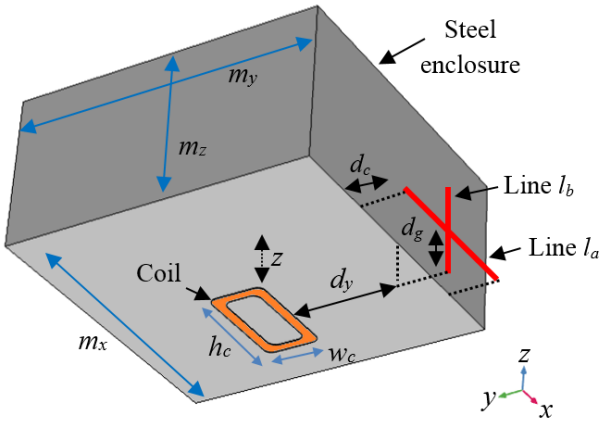

Figure 16. Setup of the simplified configuration.

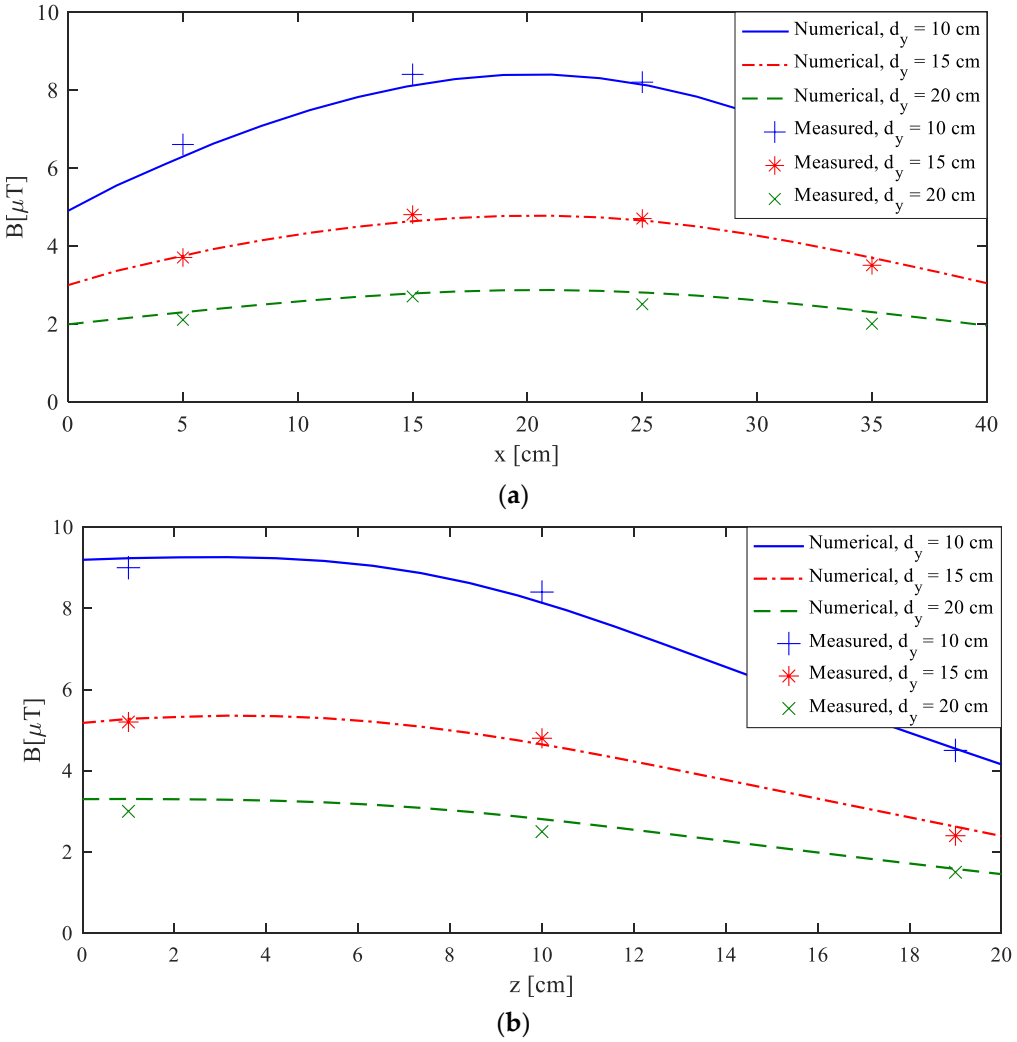

Figure 17. Calculated and measured magnetic flux density along lines l_a (**a**) and l_b (**b**) (see Figure 16).

After the validation of the numerical tool, several simulations based on the FEM solution of (13) and (14) were performed to evaluate the distribution of the magnetic field in the surrounding area of an EV during wireless charging. The coil currents in terms of rms value and phase calculated in the previous section (see Figures 14 and 15) were used as input in the FEM simulations when considering the coils/body configuration in Figure 7. The magnetic field was calculated for two coils/body configurations. In the first one, the maximum coupling factor $k = 0.148$ was adopted, assuming the coil separation of $\Delta_{z2} = 200$ mm and no misalignment ($\Delta x = \Delta y = 0$), leading to $d_x = 1.405$ m and $d_y = 0.55$ m. In the second one, the worst case coupling condition was considered, assuming $k = 0.072$ (coil vertical separation of $\Delta_{z3} = 250$ mm) and lateral offset of $\Delta x = 75$ mm and $\Delta y = 100$ mm, leading to $d_x = 1.33$ m and $d_y = 0.45$ m.

The magnetic field was calculated along the four lines shown in Figure 18:

- Line 1 (l_1): horizontal line parallel to the x axis on the side of the vehicle at a distance of $d_g = 150$ mm from the ground and $d_c = 10$ mm from the EV external side;
- Line 2 (l_2): vertical line parallel to the z axis on the external side of the vehicle at a distance of $d_c = 10$ mm from the EV external side;
- Line 3 (l_3): vertical line parallel to the z axis on the front of the vehicle at a distance of $d_c = 10$ mm from the EV external side;
- Line 4 (l_4): horizontal line parallel to the x axis inside the cabin at a distance of $d_i = 50$ mm from the cabin floor.

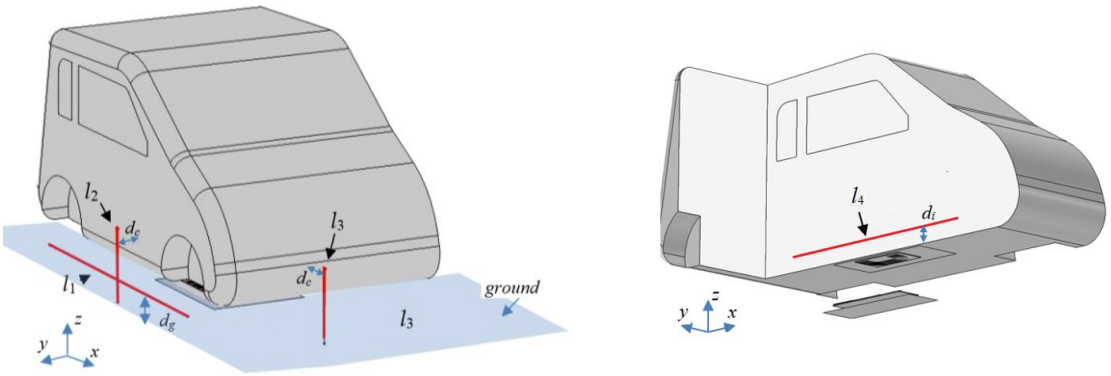

(**a**) (**b**)

Figure 18. Measurement lines of the magnetic field outside (**a**) and inside (**b**) the vehicle.

The magnetic field levels for the SS and the LCC compensations with different configurations corresponding to $k = 0.072$ and $k = 0.148$ were numerically calculated on the measurement lines, as shown in Figure 19, where the calculated values were compared with the RL of ICNIRP 1998 and 2010 guidelines. The RL in terms of magnetic flux density at the considered frequency of 85 kHz was $B_{RL} = 6.25$ µT for ICNIRP 1998 [9] and $B_{RL} = 27$ µT for ICNIRP 2010 [10]. It is important to note that compliance with ICNIRP 1998 is very relevant in Europe, since the RLs have been adopted by a Council Recommendation [40], which has legal value and has never been adjourned with ICNIRP 2010 RLs. The obtained results show the LCC compensation could achieve a significant reduction of the magnetic field compared to the SS compensation. Furthermore, with the LCC compensation, the ICNIRP 2010 RL was never exceeded in all considered cases. The significant influence of the offset and the distances d_x and d_y should be noted. Inside the vehicle (see line l_4), the magnetic field was well shielded by the VA shields and by the car bodyshell; thus, the magnetic field levels were well below the limits. For the worst case scenario ($k = 0.072$), the magnetic field maps were calculated in the three planes shown in Figure 20 and defined as:

- p_1: x-z plane beside the vehicle at a distance of $d_c = 10$ mm from the body;
- p_2: y-z plane on the front of the vehicle at a distance of $d_c = 10$ mm from the body;
- p_3: x-y plane between the coils under the vehicle at $z = 125$ mm from the ground.

Measurement planes p_1, p_2, and p_3 had square shapes with side lengths equal to 1 m. The behavior of the magnetic flux density for the SS and the LCC compensations on the three planes are shown in Figure 21. From the magnetic field maps, it is possible to see the great advantage of the LCC compensation with a significant reduction of the magnetic field in all the considered areas outside the vehicle. Critical B-values were found in the region under the vehicle between coils (see Figure 21c) as expected, but human body exposure may have been prevented by control access techniques that immediately stopped the charging process after detection of objects or living beings in this region. No problems occurred in the region outside the EV in front of the body (see Figure 21b) due to a large value of distance d_x. Thus, the main concern about health risks from EMF exposure was in the region beside the EV (see Figure 21a).

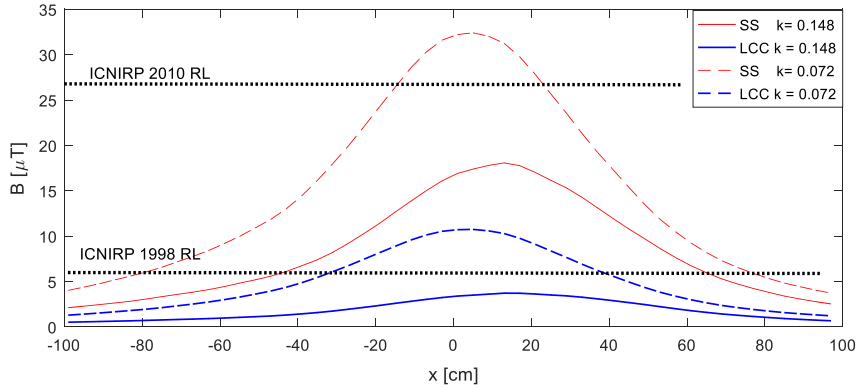

(**a**)

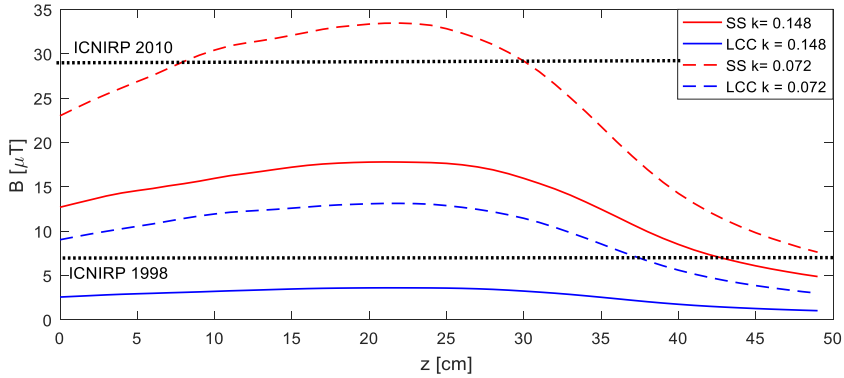

(**b**)

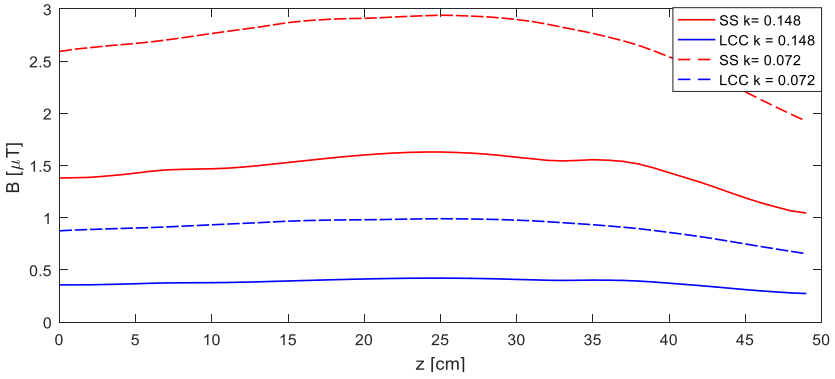

(**c**)

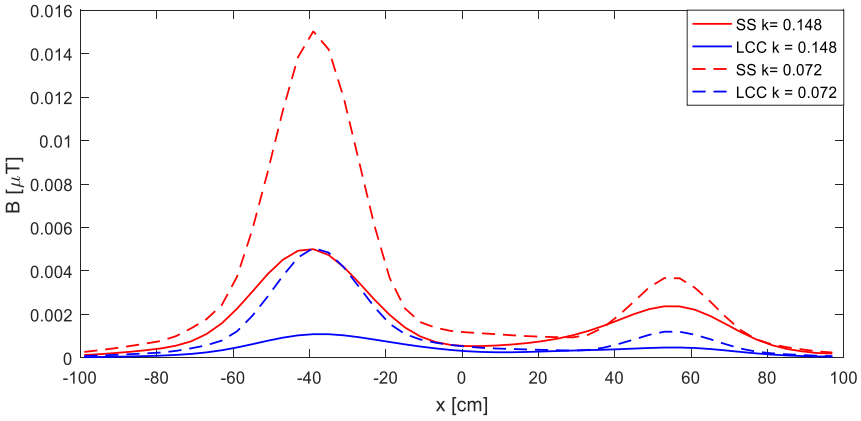

(**d**)

Figure 19. Magnetic flux density B calculated on the lines l_1 (**a**), l_2 (**b**), l_3 (**c**), and l_4 (**d**).

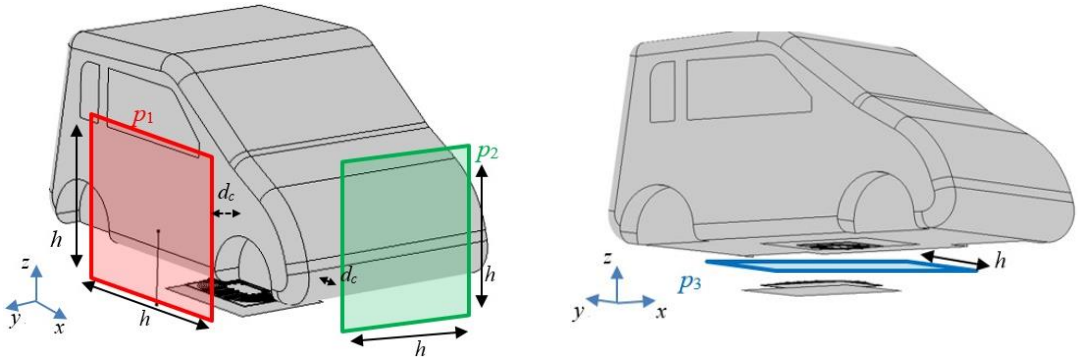

(**a**) (**b**)

Figure 20. Calculation planes for the magnetic field: p_1, p_2 (**a**) and p_3 (**b**).

Thus, the magnetic field maps were calculated in the critical plane p_1 considering three different body widths m_y. According to (21), the variation of the body width influences the distance d_y, i.e., the distance between the GA coil and the projection of the outer side of the vehicle. Thus, d_y had a very significant impact on the magnetic field in that area. The worst case condition in terms of coils distance (Δz_3 = 250 mm) and offset (Δx = 75 mm and Δy = 100 mm) was adopted. Three body widths were simulated, and the corresponding distances d_y were obtained as:

- m_y = 1.6 m d_y = 45 cm;
- m_y =1.7 m, d_y = 50 cm;
- m_y =1.8 m, d_y = 55 cm.

The behaviors of the magnetic fields for the SS and the LCC compensations on the plane p_1 are shown in Figure 22 for the three considered test cases. The obtained results for the SS and the LCC compensations highlight that body size, especially the width, had a significant influence on the magnetic field levels. Specifically, when considering the widest examined body (m_y = 1.8 m), the magnetic field beside the EV was compliant with ICNIRP 2010 RL for both SS and LCC compensations, but it was not compliant with ICNIRP'98 RL for SS compensation. For the narrowest examined body (m_y = 1.6 m), the ICNIRP 2010 RL was respected only using the LCC compensation, while the ICNIRP '98 was always exceeded.

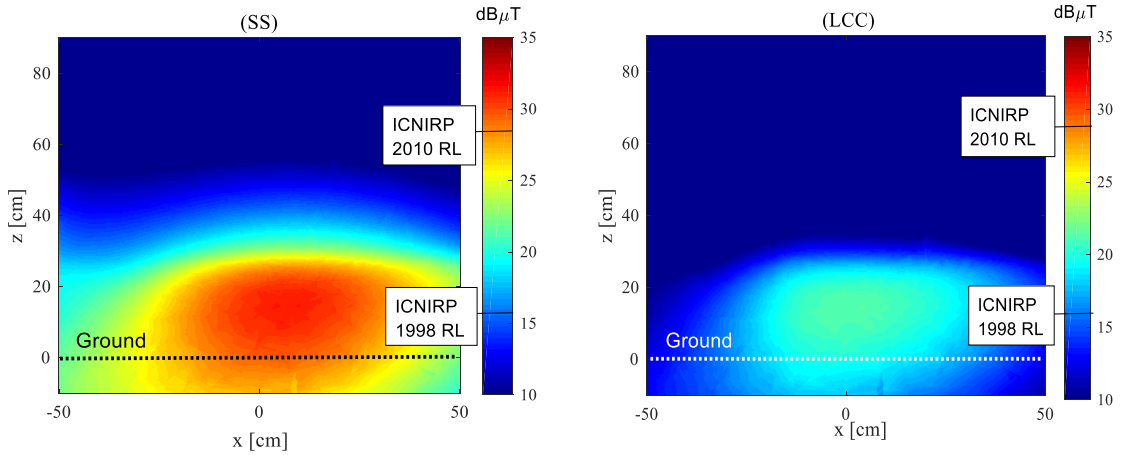

(**a**)

Figure 21. *Cont.*

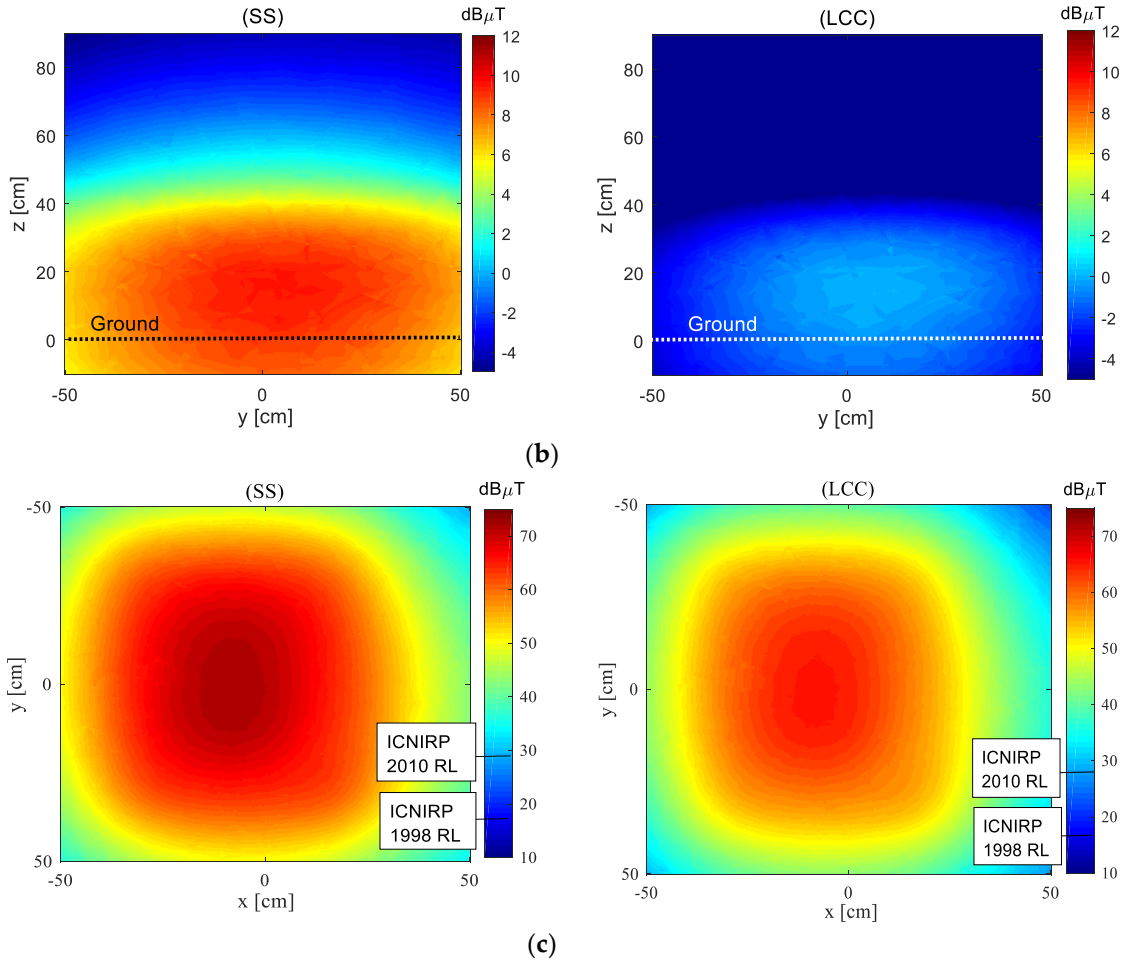

Figure 21. Maps of the magnetic flux density B (rms) on the planes p_1 (**a**), p_2 (**b**) and p_3 (**c**) for SS and LCC compensations.

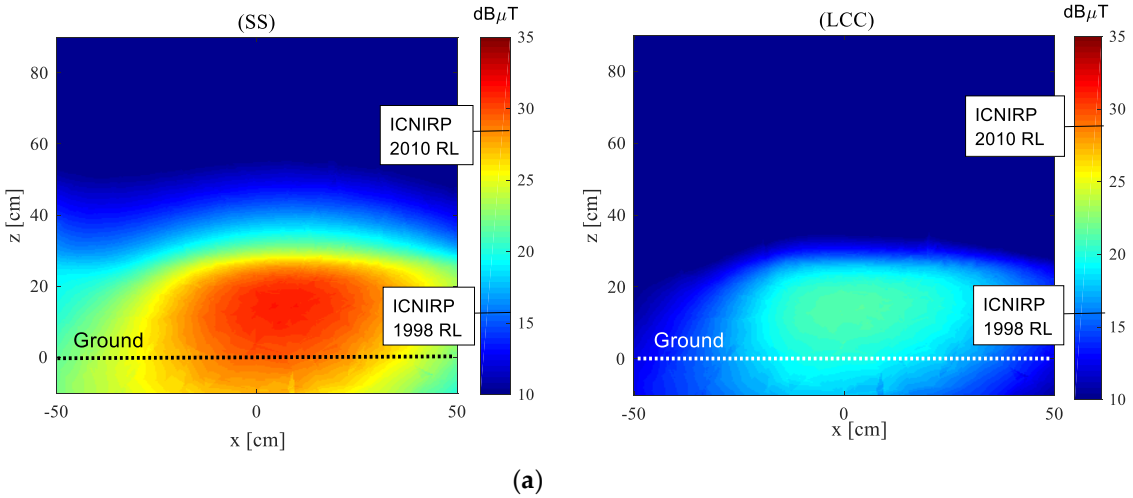

Figure 22. *Cont.*

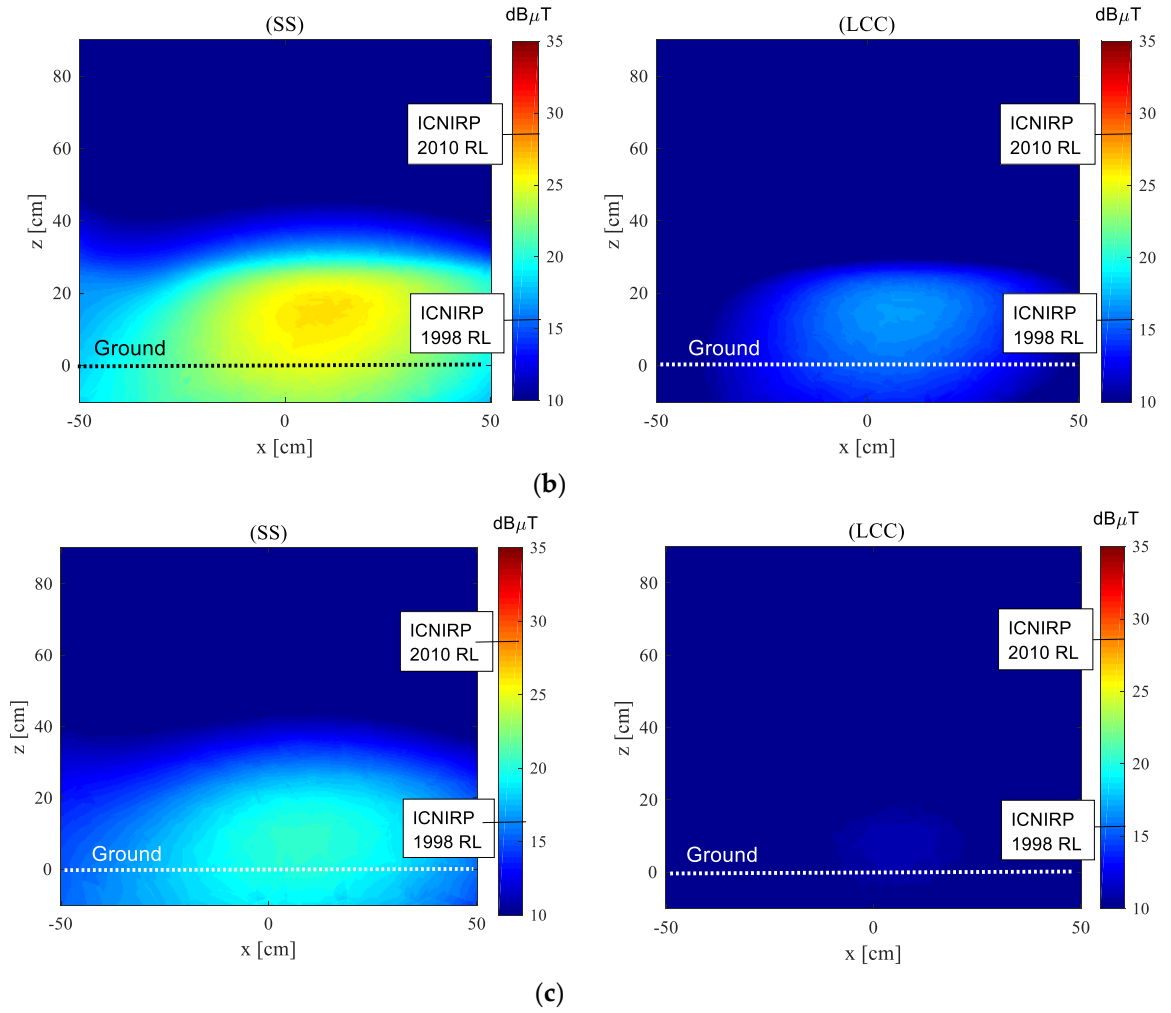

Figure 22. Maps of the magnetic flux density B (rms) on the plane p_1 for d_y = 0.45 m (**a**), d_y = 0.50 m (**b**), and d_y = 0.55m (**c**) for SS and LCC compensations.

6. Conclusions

The magnetic field behavior of an EV equipped with WPT coils during battery wireless charging was assessed by numerical simulations. The SAE RP J2954 recommendations were taken into account for the design of the WPT coils and for the admissible configurations and tolerance about coil vertical separation and lateral misalignment. The numerical simulations were carried out by a sophisticated circuit/field model. Considering a worst case scenario of a small city car with a bodyshell in steel and equipped with a Class2 WPT system (7.7 kVA), the magnetic field levels were evaluated for maximum admissible values of Z class (i.e., ground clearance) and offset (i.e., lateral misalignment). Assuming an SS compensation topology, the magnetic field beside the EV exceeded the ICNIRP 2010 RL (B_{max} = 27 μT) and the ICNIRP 1998 RL (B_{max} = 6.23 μT), while the field was compliant with both ICNIRP guidelines inside the EV. The simulations were repeated using the LCC compensation, which permitted variations in the ratio of the GA and the VA currents flowing through the coils. The obtained results show the LCC compensation achieved a significant reduction of the magnetic field compared to the SS compensation. Furthermore, with the LCC compensation, the ICNIRP 2010 RL was never exceeded beside the EV in all considered cases, while the ICNIRP 1998 RL was exceeded, but the maximum magnetic field was not far from the ICNIRP 1998 RL. Finally, the influence of the body width on the magnetic field distribution was investigated, revealing the importance of this parameter for the compliance of the ICNIRP RLs.

Author Contributions: T.C., S.C., F.M and M.F. conceived and planned the experiments. T.C. carried out the experiments. S.C., F.M and M.F. planned and carried out the simulations. All authors provided critical feedback, improved the final design, analyzed the data and wrote the paper.

Funding: This research was funded by the University of L'Aquila, RIA Project, 2018.

Conflicts of Interest: The founding sponsors had no role in the design of the study; in the collection, analyses, or interpretation of data; in the writing of the manuscript, and in the decision to publish the results.

References

1. Covic, G.A.; Boys, J.T. Inductive power transfer. *Proc. IEEE* **2013**, *101*, 1276–1289. [CrossRef]
2. Shinohara, N. Power without wires. *IEEE Microw. Mag.* **2011**, *11*, 64–73. [CrossRef]
3. Wang, C.S.; Covic, G.A.; Stielau, O.H. Power Transfer Capability and Bifurcation Phenomena of Loosely Coupled Inductive Power Transfer Systems. *Trans. Ind. Electron.* **2004**, *51*, 148–157. [CrossRef]
4. Ahmad, A.; Alam, M.S.; Chabaan, R.A. Comprehensive Review of Wireless Charging Technologies for Electric Vehicles. *Trans. Transp. Electrif.* **2018**, *4*, 38–63. [CrossRef]
5. ISO/PAS 19363:2017. *Electrically Propelled Road Vehicles—Connection to an External Electric Power Supply—Safety Requirements*; ISO: Geneva, Switzerland, 2015. [CrossRef]
6. IEC 61980-1:2015. *Electric Vehicle Wireless Power Transfer (WPT) Systems—Part 1: General Requirements*; International Electrotechnical Commission: Geneva, Switzerland, 2015.
7. SAE Recommended Practice J2954 (rev. 201711). *Wireless Power Transfer for Light-Duty Plug-In/Electric Vehicles and Alignment Methodology*; 27-11-2017; SAE International: Troy, MI, USA, 2017. [CrossRef]
8. Schneider, J.; Carlson, R.; Sirota, J.; Sutton, R.; Taha, E.; Kesler, M.; Kamichi, K.; Teerlinck, I.; Abeta, H.; Minagawa, Y.; Yazaki, S. *Validation of Wireless Power Transfer up to 11kW Based on SAE J2954 with Bench and Vehicle Testing*; SAE International: Troy, MI, USA. [CrossRef]
9. International Commission on Non-Ionizing Radiation Protection. Guidelines for limiting exposure to time-varying electric, magnetic, and electromagnetic fields (up to 300 GHz). *Health Phys.* **1998**, *74*, 494–522.
10. International Commission on Non-Ionizing Radiation Protection. Guidelines for limiting exposure to time-varying electric and magnetic fields for low frequencies (1 Hz–100 kHz). *Health Phys.* **2010**, *99*, 818–836.
11. Zhai, L.; Zhong, G.; Cao, Y.; Hu, G.; Li, X. Research on Magnetic Field Distribution and Characteristics of a 3.7 kW Wireless Charging System for Electric Vehicles under Offset. *Energies* **2019**, *12*, 392. [CrossRef]
12. Feliziani, M.; Cruciani, S. Mitigation of the magnetic field generated by a wireless power transfer (WPT) system without reducing the WPT efficiency. In Proceedings of the International Symposium on Electromagnetic Compatibility, Brugge, Belgium, 2–6 September 2013; pp. 610–615.
13. Campi, T.; Cruciani, S.; Feliziani, M. Magnetic Shielding of Wireless Power Transfer Systems. In Proceedings of the International Symposium on Electromagnetic Compatibility, Tokyo, Japan, 13–16 May 2014.
14. Feliziani, M.; Cruciani, S.; Campi, T.; Maradei, F. Near field shielding of a wireless power transfer (WPT) current coil. *Prog. Electromagn. Res. C* **2017**, *77*, 39–48. [CrossRef]
15. Campi, T.; Cruciani, S.; Feliziani, M. Numerical characterization of the magnetic field in electric vehicles equipped with a WPT system. *Wirel. Power Transf.* **2017**, *4*, 78–87. [CrossRef]
16. Campi, T.; Cruciani, S.; Feliziani, M. Wireless power transfer (WPT) system for an electric vehicle (EV): How to shield the car from the magnetic field generated by two planar coils. *Wirel. Power Transf.* **2017**, *5*, 1–8. [CrossRef]
17. Wang, Q.; Li, W.; Kang, J.; Wang, Y. Electromagnetic Safety Evaluation and Protection Methods for a Wireless Charging System in an Electric Vehicle. *IEEE Trans. Electromagn. Compat. Early Access* **2018**, 1–13. [CrossRef]
18. Moon, H.; Kim, S.; Park, H.H.; Ahn, S. Design of a resonant reactive shield with double coils and a phase shifter for wireless charging of electric vehicles. *IEEE Trans. Magn.* **2015**, *51*, 1–4. [CrossRef]
19. Kim, S.; Park, H.; Kim, J. Design and Analysis of a Resonant Reactive Shield for a Wireless Power Electric Vehicle. *IEEE Trans. Microw. Theory Tech.* **2014**, *62*, 1057–1066. [CrossRef]
20. Ding, P.; Bernard, L.; Pichon, L. Evaluation of Electromagnetic Field in Human Body Exposed to Wireless Inductive Charging System. *IEEE Trans. Magn.* **2014**, *50*, 1037–1040. [CrossRef]
21. Laakso, I.; Hirata, A. Evaluation of the induced electric field and compliance procedure for a wireless power transfer system in an electrical vehicle. *Phys. Med. Biol.* **2013**, *58*, 7583. [CrossRef] [PubMed]

22. Zhang, K.H.; Du, L.N.; Zhu, Z.B.; Song, B.W.; Xu, D.M. A Normalization Method of Delimiting the Electromagnetic Hazard Region of a Wireless Power Transfer System. *IEEE Trans. Electromagn. Compat.* **2018**, *60*, 829–839. [CrossRef]
23. Kim, S.; Covic, G.A.; Boys, J.T. Comparison of Tripolar and Circular Pads for IPT Charging Systems. *IEEE Trans. Power Electron.* **2018**, *33*, 6093–6103. [CrossRef]
24. De Santis, V.; Campi, T.; Cruciani, S.; Laakso, I.; Feliziani, M. Assessment of the Induced Electric Fields in a Carbon-Fiber Electrical Vehicle Equipped with a Wireless Power Transfer System. *Energies* **2018**, *11*, 684. [CrossRef]
25. Yan, Z.; Zhang, Y.; Song, B.; Zhang, K.; Kan, T.; Mi, C. An LCC-P Compensated Wireless Power Transfer System with a Constant Current Output and Reduced Receiver Size. *Energies* **2019**, *12*, 172. [CrossRef]
26. Ann, S.; Lee, W.Y.; Choe, G.Y.; Lee, B.K. Integrated Control Strategy for Inductive Power Transfer Systems with Primary-Side LCC Network for Load-Average Efficiency Improvement. *Energies* **2019**, *12*, 312. [CrossRef]
27. Li, S.; Li, W.; Deng, J.; Nguyen, T.D.; Mi, C.C. A double-sided LCC compensation network and its tuning method for wireless power transfer. *IEEE Trans. Veh. Technol.* **2015**, *64*, 2261–2273. [CrossRef]
28. Feliziani, M.; Campi, T.; Cruciani, S.; Maradei, F.; Grasselli, U.; Macellari, M.; Schirone, M. Robust LCC compensation in wireless power transfer with variable coupling factor due to coil misalignment. In Proceedings of the IEEE 15th International Conference on Environment and Electrical Engineering (EEEIC), Rome, Italy, 10–13 June 2015; pp. 1181–1186. [CrossRef]
29. Campi, T.; Cruciani, S.; Maradei, F.; Feliziani, M. Near Field reduction in a Wireless Power Transfer System using LCC compensation. *IEEE Trans. Electromagn. Compat.* **2017**, *59*, 686–694. [CrossRef]
30. Feliziani, M.; Maradei, F. Edge element analysis of complex configurations in presence of thin shields. *IEEE Trans. Magn.* **1997**, *33*, 1548–1551. [CrossRef]
31. Feliziani, M.; Maradei, F. Fast computation of quasi-static magnetic fields around nonperfectly conductive shields. *IEEE Trans. Magn.* **1998**, *34*, 2795–2798. [CrossRef]
32. Buccella, C.; Feliziani, M.; Fuina, V. ELF magnetic field mitigation by active shielding. In Proceedings of the IEEE International Symposium on Industrial Electronics ISIE-02, L'Aquila, Italy, 8–11 July 2002. [CrossRef]
33. Feliziani, M.; Cruciani, S. FDTD modeling of impedance boundary conditions by equivalent LTI circuits. *IEEE Trans. Microw. Theory Tech.* **2012**, *60*, 3656–3666. [CrossRef]
34. Feliziani, M.; Maradei, F.; Tribellini, G. Field analysis of penetrable conductive shields by the finite-difference time-domain method with impedance network boundary conditions (INBCs). *IEEE Trans. Electromag. Compat.* **1999**, *41*, 307–319. [CrossRef]
35. Feliziani, M. Subcell FDTD modeling of field penetration through lossy shields. *IEEE Trans. Electromag. Compat.* **2012**, *54*, 299–307. [CrossRef]
36. Feliziani, M.; Cruciani, S.; Campi, T.; Maradei, F. Artificial Material Single Layer to Model the Field Penetration Through Thin Shields in Finite-Elements Analysis. *IEEE Trans. Microw. Theory Techn.* **2018**, *66*, 56–63. [CrossRef]
37. Cruciani, S.; Campi, T.; Maradei, F.; Feliziani, M. Conductive Layer Modeling by Improved Second-Order Artificial Material Single-Layer Method. *Trans. Antennas Propag.* **2018**, *66*, 5646–5650. [CrossRef]
38. Cruciani, S.; Campi, T.; Maradei, F.; Feliziani, M. Artificial material single-layer method applied to model the electromagnetic field propagation through anisotropic shields. *IEEE Trans. Microw. Theory Tech.* **2018**, *66*, 3756–3763. [CrossRef]
39. Spadacini, G.; Grassi, F.; Pignari, S.A. Modelling and simulation of conducted emissions in the powertrain of electric vehicles. *Prog. Electromagn. Res. B* **2016**, *69*, 1–15. [CrossRef]
40. European Council Recommendation of 12 July 1999 on the Limitation of Exposure of the General Public to Electromagnetic Fields (0 Hz to 300 GHz) (1999/519 CE). Available online: http://data.europa.eu/eli/reco/1999/519/oj (accessed on 18 April 2019).